THE JOURNAL OF PHYSICAL CHEMISTRY C

pubs.acs.org/JPCC Article

Carrier Density, Effective Mass, and Nuclear Relaxation Pathways in Plasmonic Sn:In_2O_3 Nanocrystals

Carl R. Conti III, Giovanni Quiroz-Delfi, Joanna S. Schwarck, Banghao Chen, and Geoffrey F. Strouse*

Cite This: J. Phys. Chem. C 2020, 124, 28220–28229 Read Online

ACCESS | Metrics & More | Article Recommendations | Supporting Information

ABSTRACT: Correlating changes in carrier density arising from incorporating dopant ions into the lattice of a plasmonic semiconductor nanocrystals (NCs) with the observed physical properties at the elemental level can improve our understanding of these materials. Here, we investigate Sn:In_2O_3 (ITO) NCs, a well-known near-infrared plasmonic system, by analyzing the induced carrier density changes that occur in the optical response and the ^{119}Sn nuclear relaxation rates. The carrier density, as evaluated by a chemical titration method, is correlated to the Burstein–Moss shift and the plasmon frequency to evaluate the effectiveness of the Drude-Lorentz model. Comparison of the values for carrier density extracted from these methods suggests the Drude and Burstein–Moss models underestimate the actual carrier density, particularly at higher concentrations, and that the parabolic approximation to the band structure is not appropriate for the ITO samples. The error in the fits can be accommodated using a modification in the Drude-Lorentz model to incorporate an additional correction value to account for the change in the local band shape as the Fermi level is moved with increasing carrier incorporation. The chemical shift and broadening of the ^{119}Sn solid-state NMR features provide a direct measure of the effects of carrier density on nuclear spin relaxation pathways. The ^{119}Sn signal of ITO NCs exhibits an increase in the full width at half-maximum with increasing carrier density, which can be related to the carrier-dependent T_2* effects. The experimental results indicate the simple models are empirically predictive but require further evaluation to be quantitative.

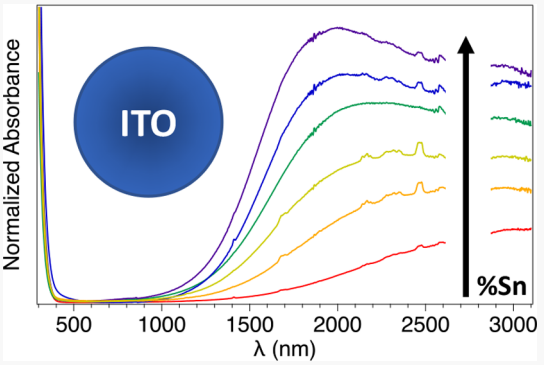

INTRODUCTION

A growing interest in plasmonic semiconductor nanocrystals (PSNCs) generated by aliovalent doping of wide band gap semiconductors has appeared due to the observation that the localized surface plasmon resonance (LSPR) frequency and extinction are directly dependent on the carrier density at the Fermi level.[1−8] In PSNCs, the LSPR extinction feature arises from the coherent oscillation of carriers introduced at the Fermi level by carrier delocalization into the valence (p-type) or conduction (n-type) band upon doping. LSPRs are well-known in coinage metals, where the carriers are treated as a Fermi gas and an extinction feature in the visible regime is observed that is dampened by electron–electron and electron–phonon interactions.[9−16] The observed frequency is attributed to the interference of the real and imaginary terms of the dielectric function. In PSNCs, the LSPR feature is highly tunable but occurs in the infrared instead of the visible due to their lower carrier density when compared to metals such as Au and Ag.[1,4,17,18]

The incorporation of n- and p-type dopants into semiconductors results in changes to the Fermi level and should produce changes in the UV–vis (band edge) and NMR features that scale with carrier density. A shift in the band edge absorption has been observed in degenerately doped n- and p-type semiconductors and should appear in aliovalent doped metal oxides that exhibit an LSPR. The absorption shift arises from the nonzero occupancy of states at the conduction band minimum that scales with carrier density, which results in a change to the energy required to excite an electron from the valence band into the conduction band.[19,20] The change in energy can be fit to the Burstein–Moss expression, and the shift in the optical band gap is treated as a Coulombic repulsion term renormalizing the band gap.[21−24] In terms of NMR, free carriers can induce changes to the nuclear relaxation rates (T_1 and T_2), due to a paramagnetic relaxation enhancement, as well as shift the NMR resonance by altering the local electric shielding due to an induced metallic character of the observed nuclei.[25,26]

Optical methods are convenient for carrier analysis within a sample; however, such methods require approximations to extract actual carrier density. The LSPR shift with carrier

Received: October 19, 2020
Revised: November 25, 2020
Published: December 10, 2020

https://dx.doi.org/10.1021/acs.jpcc.0c09448
J. Phys. Chem. C 2020, 124, 28220–28229

density has been shown to be adequately fit by the Drude-Lorentz model for Sn:In_2O_3 (ITO) NCs at less than 10% donor incorporation.[18,27] Although the LSPR fit follows the square root of dopant concentration, as expected from the Drude-Lorentz model, recent studies have questioned whether the extraction of carrier densities from the model is accurate.[28,29] Millstone and co-workers reported that the carrier densities extracted from the Drude model were inconsistent with a ^{77}Se solid-state nuclear magnetic resonance (ssNMR) analysis of a Knight shift and decreasing T_1 relaxation rates in vacancy-doped $Cu_{2-x}Se$.[29−31] Beaulac and co-workers suggested in InN that chemical titration is necessary to accurately measure the carrier densities in PSNCs.[28] Although correlations between each method and carrier densities have been observed, accurately measuring carrier densities using chemical titrations can allow for direct correlation of the physical properties observed by carrier-induced band edge shift, LSPR changes, and NMR effects. Comparison of the change in the LSPR[1,32,33] and the shift in the band gap absorption edge[19,22,24] as a function of the actual carrier density may allow the incorporation of a correction factor in analogy to the use of a dampening term (Γ) to explain the size-dependent plasmon response in gold.[10] By comparing the chemically measured carrier density to the observed plasmon frequency, band edge energy, and NMR properties, a correlated picture of the physical property changes that occur with increasing dopant concentration can be evaluated.

In this manuscript, the electronic and nuclear perturbations that arise from changes in the Fermi level upon incorporating an aliovalent ion into a semiconductor lattice is evaluated in spherical, oleic acid-passivated, $Sn_xIn_{2-x}O_3$ (ITO, 5 ± 0.5 nm). The carrier density, as measured by chemical titration with a one-electron oxidant, is compared to the observed spectral shifts in the NIR LSPR, the absorption edge in the UV−vis, and the ^{119}Sn NMR resonance. Analysis of the LSPR shift using the Drude model and the absorption band edge shift via the Burstein−Moss relationship reveal that, while the anticipated relationships with carrier density are observed for the optical features, both models either underpredict the carrier density or require a correction term to be quantitative. A linear dependence of the ^{119}Sn line width and Knight shift on carrier density is observed in the ^{119}Sn NMR spectra. The small Knight shift (<10 ppm) most likely reflects the band structure lacking Sn s-orbital contributions in the conduction band. The observed linear dependence on the NMR line width for the ^{119}Sn features with carrier density indicates that the T_2 relaxation is enhanced with increased carrier density. This behavior is anticipated in n-type ITO NCs, confirming the chemical titration values are valid. Although T_1 is also an important relaxation pathway, T_1 is observed to be too long to be directly measured for the Sn:In_2O_3. The experimental observations are consistent with the expectation that when Sn(IV) is doped into In_2O_3, the presence of carriers at the Fermi level will impact the optical spectra and nuclear spin relaxation rate due to a paramagnetic enhancement.

This study allows a direct correlation of carrier density measured by chemical titration with the observed changes in the optical and NMR spectral response to increasing carrier density in ITO NCs and illustrates the power of ssNMR to act as a local probe in plasmonic systems, providing a deeper insight into structure and carrier relaxation pathways. The study extends the use of ssNMR probe methods to analyze commercially relevant ITO NCs in an important step to developing a full understanding of the plasmonic behavior outside of the confinement limit and the role of T_2 on carrier relaxation in an n-type semiconductor induced by aliovalent doping. Developing probe techniques that measure carrier density and carrier relaxation rates is important for the continued development of electrochromic windows,[34,35] photocatalysis,[36,37] and biomedical treatments.[38,39]

MATERIALS AND METHODS

Indium(III) acetate ($In(OAc)_3$, 99.99%), oleic acid (90%, technical grade), 1,2,4,5-tetrafluorobenzene ($C_6H_2F_4$, 99%), and tetrachloroethylene (spectrophotometric grade, 99+%) were purchased from Alfa Aesar. Tin acetate ($Sn(OAc)_4$, 98%) and chloroform (high-performance liquid chromatography (HPLC) grade) were purchased from Thermo Fisher Scientific. Oleyl alcohol (80−85%, technical grade) and nitrosonium tetrafluoroborate ($NOBF_4$) were purchased from Beantown Chemical. Acetone (≥99.5%), ethanol (95%), acetonitrile (≥99.9%, anhydrous), and nitric acid (67−70%, for trace metal analysis) were purchased from VWR. Toluene (≥99.5%) was purchased from Sigma-Aldrich. Tin acetate was dried in a vacuum oven at 120 °C for 4 h prior to use and stored in a desiccator. Tetrachloroethylene was stored with 3 Å molecular sieves. All other chemicals were used as received.

Synthesis of X% ITO Nanocrystals. ITO nanocrystals (NCs) of various doping concentrations were synthesized as previously reported by Hutchison and co-workers.[40] Metal oleate precursors are formed in oleic acid under N_2 and then added dropwise at a rate of 0.2 mL/min to 12.5 mL of oleyl alcohol kept at 230 °C, while N_2 is continuously run over the reaction. After the injection is complete, the solution was kept at 230 °C for an additional 20 min, followed by cooling to RT and isolation/cleanup of the NCs using toluene/acetone (three times) and centrifugation.

Elemental Analysis. Inductively coupled plasma-mass spectrometry (ICP-MS) was performed using a Thermo Scientific iCAP RQ ICP-MS to confirm the ratio of Sn/In in the NCs. Samples were digested in concentrated nitric acid and then diluted to 2% HNO_3. Calibration curves were prepared from serial dilutions of a Sn/In standard dissolved in 2% nitric acid with R^2 values greater than 0.999 for both ions. Each sample was measured in triplicate after an initial survey run, and there was a minimum of 30 s wash time between samples.

Powder X-ray Diffraction (pXRD). pXRD patterns were collected with a Rigaku MiniFlex powder X-ray diffractometer using Cu Kα. Samples were dried out, crushed into a fine powder, and then loaded onto a zero-background micro-powder plate. Scans were collected from 15 to 80° 2θ at a rate of 5°/min and a 0.1° step size. Whole powder pattern fitting and the Halder-Wagner method for Scherrer analysis were completed using the Rigaku SmartLab Studio software and performed for all ITO NCs.

Transmission Electron Microscopy (TEM). Nanocrystal samples were diluted and suspended in chloroform and then dropcast onto Formvar-coated copper TEM grids (Ted Pella) and allowed to dry in a desiccator overnight. Experiments were performed at the National High Magnetic Field Laboratory using a JEM-ARM200cF electron microscope operating at 200 kV.

UV−Vis−NIR Spectroscopy. Purified ITO NCs were suspended in tetrachloroethylene. UV−Vis−NIR data were collected using a PerkinElmer Lambda 950 spectrophotometer. A 1 cm path length NIR quartz cuvette from Spectrocell was

https://dx.doi.org/10.1021/acs.jpcc.0c09448
J. Phys. Chem. C 2020, 124, 28220−28229

used for all absorption experiments. Spectra were baseline-corrected using neat tetrachloroethylene and normalized to the band edge absorption of the ITO NCs.

$NOBF_4$ Titrations. The one-electron oxidation of the ITO NCs was adapted from ref 28. A known concentration of purified ITO NCs was suspended in dry tetrachloroethylene and brought into an inert atmosphere glovebox. A known concentration of $NOBF_4$ in MeCN was titrated into the ITO suspension and left to oxidize for 30 min. The sample was then loaded into a Pike Technologies liquid Fourier transform infrared (FTIR) cell with BaF_2 windows and a path length of 0.5 mm. FTIR measurements were performed in transmission mode using a Jasco 6800 FTIR spectrometer. This procedure was repeated until the LSPR absorbance did not decrease upon oxidation. The absorbance at each titration point was integrated in order to account for changes in the shape of the LSPR. The linear region of the titration was then extrapolated to determine the amount of $NOBF_4$ theoretically required to completely extract all free carriers. This number was then converted to the carrier density of the ITO NCs by dividing the extracted number of electrons by the volume of NCs in the suspension calculated using the density of indium oxide and the size of the NCs.

Solution NMR Spectroscopy. Solution ^{19}F NMR was performed using a 400 MHz Bruker AVIII spectrometer. The concentration of the $NOBF_4$ in MeCN solution was determined using a known concentration of 1,2,4,5-tetrafluorobenzene as an internal standard and by measuring the ratio of the integrated $NOBF_4$ feature to that of the tetrafluorobenzene signal.

Solid-State NMR Spectroscopy. Dried nanocrystals were crushed into a fine powder and packed into a 4 mm zirconia rotor. A 500 MHz Bruker AVIII HD wide-bore spectrometer was used for all measurements. Spectra were collected using a standard spin−echo pulse sequence with a pulse width of 6.4 μs, an acquisition time of 5.5 ms, and 24 576 scans for each sample at the ^{119}Sn Larmor frequency 186.49 MHz. The chemical shifts were referenced to solid SnO powder at −206 ppm. Magic-angle spinning was used for all samples at a rate of 10 kHz.

RESULTS AND DISCUSSION

A series of oleic acid-passivated 5.0 ± 0.5 nm $Sn_xIn_{2-x}O_3$ (ITO) (x = 0.020, 0.031, 0.040, 0.050, 0.063, and 0.073) NCs were prepared following the synthetic protocol of Hutchison and co-workers.[40] The Sn concentrations were verified by ICP-MS. pXRD allows an assignment of all samples to the bcc bixbyite phase (PDF No. 03-065-3170) (Supporting Figure S1). There are no discernible pXRD shifts in the diffraction peaks, and calculations of the lattice parameter for each sample showed little to no change, owing to the similarity in size of the In(III) and Sn(IV) ions ($r_{In(III)}$ = 81 pm; $r_{Sn(IV)}$ = 71 pm).[41] Scherrer analysis of the NCs using the Halder-Wagner method and whole powder pattern fitting is provided in Table S1. The size was confirmed by TEM imaging, where the ITO NCs are observed to be spherical with lattice fringes assignable to the d-spacing for the (222) facet of the bixbyite crystal structure (d = 2.93 Å). All analytical data for the ITO series are available in the Supporting Information.

Carrier Density in ITO. The carrier density of the ITO samples prepared in this study was quantified by chemical titration with $NOBF_4$, a one-electron oxidant. The use of $NOBF_4$ to evaluate carriers was previously reported for InN by Beaulac and co-workers.[28] In Figure 1, a plot is shown of the carrier concentration determined via chemical titration versus %Sn incorporation into In_2O_3 measured by ICP-MS. The linear relationship confirms that dopant concentration is directly proportional to the carrier density of the ITO NCs within this regime (2.0−7.3%). The dependence of carrier density on Sn(IV) doping is consistent with earlier studies suggesting the Sn(IV) incorporation into In_2O_3 is stochastic across the entire nanocrystal volume and exhibits equivalent dopant activation within this doping range based on the LSPR shift.

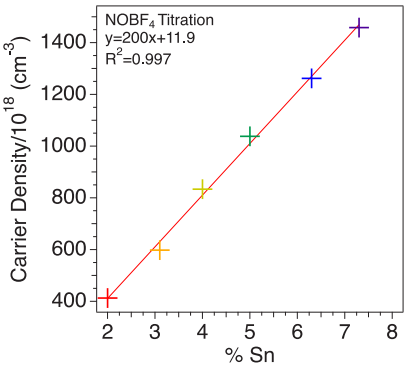

Figure 1. Carrier density determined by one-electron oxidant $NOBF_4$ titrations for 2.0−7.3% ITO NCs.

Evaluation of the plot reveals that the carrier density is in the range of (0.4−1.4) × 10^{21} cm^{-3} or 27−95 electrons per NC. It is expected that one free carrier will be generated per Sn dopant incorporated into In_2O_3, but the measured carrier density values indicate that only 0.65 free carriers are generated per Sn dopant. The observed 35% dopant deactivation is attributed to compensating defect complexes within the NC arising from inherent oxygen vacancies within the bixbyite crystal structure that produces oxygen interstitial complexes of the form $2Sn_{In}\cdot-O_i''$.[42,43] It is worth noting that the titration experiment is in excellent agreement with the previously reported less than 70% dopant activation in ITO NCs.[43] Such deactivation may also arise from the existence of a surface depletion region, where surface defects result in decreased free carrier generation.[44] Further evaluation allows the intrinsic carrier density to be established in the ITO samples. Native carriers in the undoped In_2O_3 NCs are expected to be present due to inherent oxygen vacancies.[42,43] From the chemical titration plot, the intrinsic carrier density can be estimated by extrapolating the plot to 0% Sn, yielding a value of 1.2 × 10^{19} cm^{-3} or 0.78 intrinsic carriers per NC from native defects in the ITO samples.

Carrier-Induced LSPR Shift. In Figure 2a, the LSPR extinction feature, as measured via UV−vis−NIR, is observed to shift to higher frequency with increasing Sn concentration. Full FTIR spectra of each sample are available in the Supporting Information (Figure S2). Since LSPRs are inherently interfacial and dielectric phenomena, the Drude-Lorentz free-electron model is typically used to model their absorbance in order to extract useful information.[21,27,45]

$$\varepsilon(\omega) = \varepsilon_\infty + \varepsilon_{BG}(\omega) + \varepsilon_{UV}(\omega) + \varepsilon_{vis}(\omega) + \varepsilon_D(\omega) \quad (1)$$

$$\varepsilon_D(\omega) = -\frac{\omega_p^2}{\omega^2 + i\omega\Gamma} \omega_p = \sqrt{\frac{ne^2}{m^* \varepsilon_0}} \quad (2\text{-}3)$$

https://dx.doi.org/10.1021/acs.jpcc.0c09448
J. Phys. Chem. C 2020, 124, 28220−28229

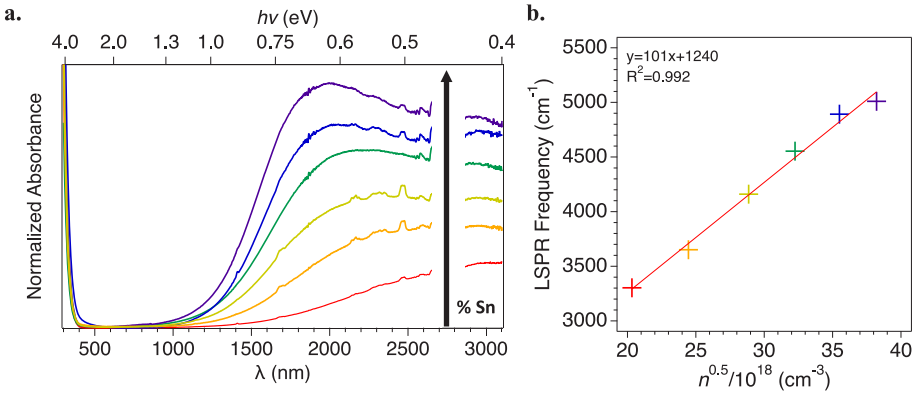

Figure 2. (a) UV−Vis−NIR of ITO NCs with increasing %Sn. Data from 2700 to 2850 nm was removed for visual clarity. (b) Square root of carrier density measured via $NOBF_4$ titration vs LSPR frequency.

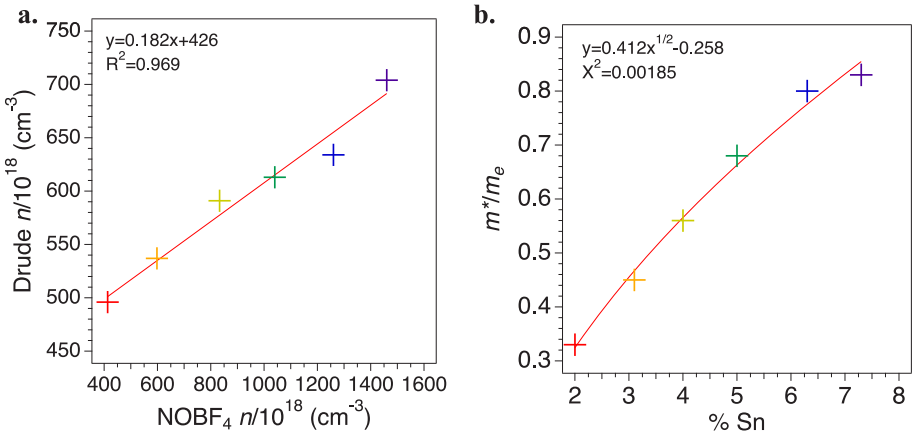

Figure 3. (a) Carrier density determined by one-electron oxidant $NOBF_4$ titrations for 2.0−7.3% ITO NCs. (b) m^* values for each ITO sample calculated using the Drude model and chemical titration-determined carrier densities.

Eq 1 represents the sum of dielectric contributions including the high-frequency dielectric constant (ε_∞) and the background, UV, visible, and Drude terms, respectively. The Drude contribution is responsible for the LSPR absorption feature and can be described using the plasma frequency (ω_p) and a dampening term (Γ). ω_p can be further broken down as shown in eq 3, where n is the free carrier density, e is the charge of the free carrier, m^* is the effective mass of the carrier, and ε_0 is the permittivity of free space. It is worth noting that the experimentally measured LSPR frequency of a nanocrystalline sample (ω_{LSPR}) can be described by the following equation,[45]

$$\omega_{LSPR} = \frac{\omega_p}{\sqrt{\varepsilon_\infty + 2}} \tag{4}$$

where ε_∞ = 4.08 for In_2O_3,[46] resulting in the observed LSPR will appear at ∼2.45 times lower frequency than the calculated ω_p.

From eqs 1−4, the values of ω_p and, therefore, ω_{LSPR} will be directly proportional to the square root of n. A plot of the LSPR shift as a function of the square root of carrier concentration extracted from the chemical titration is shown in Figure 2b. The plot of LSPR frequency versus %Sn is available in the Supporting Information (Figure S3). The values for ω_{LSPR} were determined via a Drude modeling of the absorption data using Matlab code written by the Milliron group.[27] The linear dependence of the LSPR frequency with the square root of carriers is consistent with earlier findings;[47] however, extraction of the carrier densities from LSPR data using eqs 1−4 is inconsistent with the values obtained from chemical titration (Figure 3a). The linear relationship confirms the LSPR shift is due to free carriers, but the difference in carrier density requires a correction factor of γ = 0.18. This suggests the Drude-Lorentz model underestimates the carrier densities by nearly 20%, most likely due to an additional dampening term being required, analogous to a Drude-Lorentz analysis of metallic plasmonic systems.

Such a correction term for PSNCs has been previously proposed by Jung and Pedersen[45] to account for large deviations in the calculated ω_p for ZnO when using a simple effective mass approach compared to the full band structure calculations. They proposed an advanced effective mass model of ω_p, which contained a correction term to eq 3 in order to account for the deviation.

$$\omega_p^2 = \frac{e^2 n}{\varepsilon_0 m^*} \frac{1}{\sqrt{1 + (9\pi^2 n)^{2/3} \hbar^2/(m^* \alpha)}} \tag{5}$$

In this equation, α is the correction factor that accounts for the change in local band shape as the Fermi level moves further into the conduction band with increases in n-type doping.

To evaluate the model of Jung and Pederson for the ITO samples, the effective mass of the free carriers for each ITO sample is extracted from the LSPR data using eqs 1−4 (Figure 3b). This plot shows that the value for m^* varies substantially with Sn loading, ranging from 0.33m_e at low doping levels to

https://dx.doi.org/10.1021/acs.jpcc.0c09448
J. Phys. Chem. C 2020, 124, 28220−28229

$0.83m_e$ (where m_e is the mass of an electron) at higher concentrations. The unexpected variance is in disagreement with prior results from ITO thin films and cyclotron resonance measurements on ITO NCs that confirm m^* values are $0.4m_e$ at low doping levels.[5,48,49] By combining the values of ω_P extracted from optical measurements, n measured via $NOBF_4$ titrations, and the literature value of m^* for ITO ($0.4m_e$), the Jung-Pederson model (eq 5) can be used to calculate a suitable correction factor (α) for each sample. These results are illustrated in Figure 4 and show that different correction factors were required in order to model the experimental results. The high carrier density samples (6.3%, 7.3% ITO) show that α converges to a value of 1.48 eV, while lower carrier density samples approach the simple effective mass calculation (i.e., no correction factor). The modeling for the 2.0% ITO is omitted from Figure 4 due to this convergence with the simple effective mass model.

The high carrier density limit of 1.48 eV is notable, as it agrees well with the value of 1.52 eV calculated by Jung and Pedersen for n-type ZnO.[45] However, one would expect a consistent value of α for all samples if free carrier concentration was the only variable. The shift from the uncorrected Drude model to the convergence of high carrier density samples at 1.48 eV for the advanced effective mass model indicates that there are more variables involved in this process than just carrier density. When the Fermi level lies close to the conduction band minimum, m^* is equal to the known value of $0.4m_e$, and the uncorrected Drude model can effectively explain the optical data. Once the Fermi level passes deep enough into the conduction band, as is the case for the samples with high carrier densities, the value for α ceases to change, and the advanced effective mass model can accurately describe the change in parabolicity of the band structure with a constant m^* of $0.4m_e$.

Carrier-Induced Burstein–Moss Shift. A Burstein–Moss (B-M) shift is often observed in degenerately doped semiconductors. This shift has not been widely considered for PSNCs; however, it is anticipated that a B-M shift of the absorption edge will occur in the ITO samples due to the shift in the Fermi level relative to the valence band maximum with increasing n-type dopants.[19,20] B-M shifts for thin-film ITO have been reported to be proportional to the carrier density, and they can be fit to the B-M expression

$$\Delta E_{abs} = E_g^{Sn} - E_g^0 = \left(\frac{\hbar^2}{2m^*}\right)(3\pi^2 n)^{2/3} \quad (6)$$

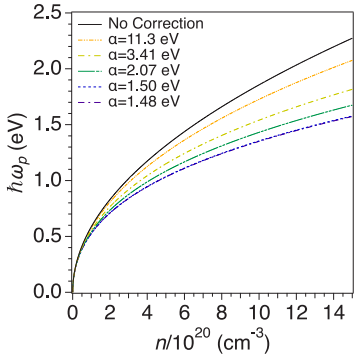

Figure 4. Dirac effective mass modeling of 3.1–7.3% ITO NCs (dashed lines) and simple effective mass model (solid line).

where E_g^{Sn} is the measured bandgap as a function of %Sn, and E_g^0 is the native bandgap at the intercept when %Sn = 0, n/m^* remain the carrier density and effective mass of the free carrier, respectively.[22,24] The B-M expression can be used to analyze the relative change in carrier density with Sn doping and can also be used to extract an average value of m^* for the series of ITO NCs.

In Figure 5a, the band edge shift with increasing Sn incorporation is plotted in the form of a Tauc plot. In a Tauc plot, the product of the absorbance and energy of light raised to $1/r$ $[(\alpha h\nu)^{1/r}]$ is plotted against $h\nu$.[50] A value of $r = 1/2$ is used for a direct band gap semiconductor like ITO, where the interband absorption is allowed.[50] The value of E_g is obtained by extrapolating the linear region of the plot. Plotting E_g versus $n^{2/3}$ (Figure 5b) shows the expected linear correlation predicted by the B-M shift. As observed in Figure 5b, the shift in E_g with increasing carrier density for each ITO sample follows the anticipated 2/3 power law with a y-intercept value of $E_g^0 = 3.16$ eV. A plot of the optical E_g shift with increasing % Sn is available in Figure S4. This 2/3 power law behavior with increasing carrier density is consistent with previous literature reports for ITO thin films[23,51,52] and is due to the parabolic nature of the conduction band minimum in In_2O_3. The average m^* for the ITO NCs can be determined using eq 6 and the slope extracted from the linear fitting in Figure 5b. This leads to a value of $0.78m_e$, which is inconsistent with the expected value for ITO. The overestimation of m^* by a parabolic band theory confirms the analysis via the Drude model showing that a loss of parabolicity in the band structure is likely occurring as the Fermi level moves further from the conduction band minimum. Analogous to the extraction of m^* using the standard Drude model, a correction factor is needed to accurately determine the m^* of a system using the Burstein–Moss shift. For 5 nm ITO NCs, this leads to a value for the correction term (defined here as Ω) being equal to 0.51.

Carrier-Induced Changes in Spin Relaxation. The extrapolation of early efforts to correlate a Knight shift and changes in T_1 with carrier density by Schmidt-Rohr in $Ag_{1-y}Pb_{18}Sb_{1+z}Te_{20}$[31] and more recently by Millstone in $Cu_{2-x}Se$[29] suggests ssNMR methods are more effective for understanding carrier behavior. To evaluate the possible discrepancy in the optical methods in ITO NCs, ^{119}Sn magic-angle spinning (MAS) ssNMR measurements were performed on the powdered samples of the ITO NCs. For these studies, samples were packed into a 4 mm zirconia rotor and spun at the magic angle at 10 kHz. The ^{119}Sn experimental data were collected using a spin–echo pulse sequence. The choice of measuring ^{119}Sn rather than ^{115}In is due to ^{119}Sn being a dipolar nucleus and because the low concentration of ^{119}Sn leads to the elimination of dipolar–dipolar coupling. ssNMR also has the advantage over optical methods in that the participation of deactivated (pinned carriers) can be directly probed by an inspection of the observed NMR features.[53,54]

The ^{119}Sn spin–echo MAS NMR spectra for the ITO series are presented in Figure 6a. The feature between −500 and −600 ppm is assigned to a six-coordinate Sn(IV) center. As % Sn increases, the assigned feature is observed to increase in intensity, shift slightly downfield (higher ppm), and broaden. It is worth noting that additional structure in the ssNMR spectrum reflects contributions that scale inversely with %Sn and arise from noise and the probe feedback that are observable due to poor signal-to-noise ratio (S/N) associated with the low concentration and natural abundance (8.6%)[53] of

https://dx.doi.org/10.1021/acs.jpcc.0c09448
J. Phys. Chem. C 2020, 124, 28220–28229

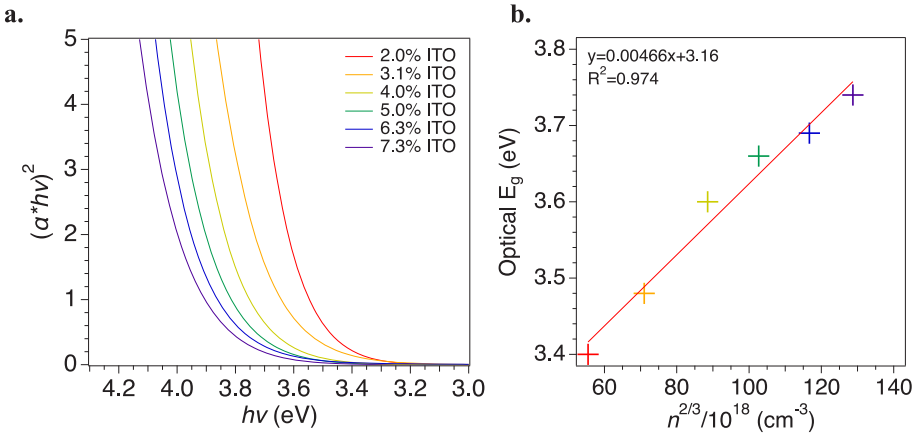

Figure 5. (a) Direct band gap Tauc plot of 2.0−7.3% ITO NCs (b) Plot of the optical bandgap vs chemical titration measured carrier density raised to the 2/3 power.

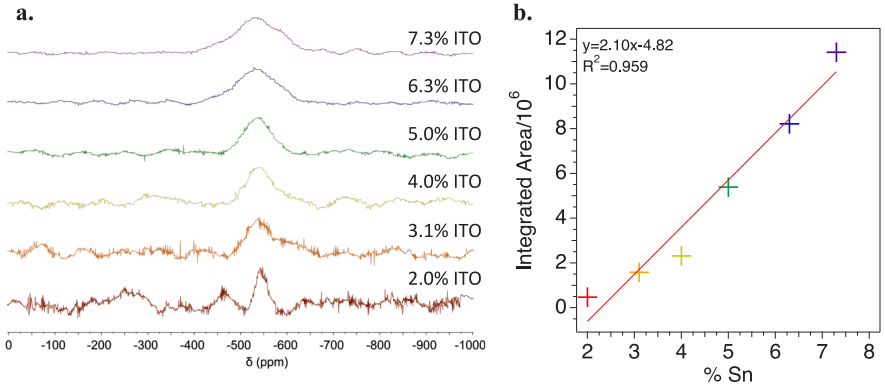

Figure 6. (a) ^{119}Sn MAS ssNMR spectra of *X*% ITO NCs. Data were collected using a spin−echo pulse sequence on a Bruker WB 500 MHz ssNMR spectrometer. Peak intensities are normalized for visual clarity. (b) Absolute integrated areas of the ^{119}Sn feature for 2.0−7.3% ITO NCs.

Sn dopant. The overall intensity of the ^{119}Sn feature increases linearly with %Sn (Figure 6b), as expected, since S/N is directly proportional to the number of nuclear spins present in the sample.[26] Many factors can influence the total integrated area of an ssNMR spectrum; therefore, comparing the integrated areas is often unreliable when compared to using this method for solution NMR. This analysis serves only to further demonstrate that the ICP-MS confirmed a trend of increasing %Sn in the PSNCs.

The observed linear downfield shift (Figure 7a) and change in the full width at half-maximum (fwhm) (Figure 7b) of the ^{119}Sn feature as a function of Sn(IV) concentration can be understood by considering that each Sn(IV) incorporation leads to a carrier at the Fermi level interacting with the ^{119}Sn nuclear spin, allowing assignments of the change in chemical shift as a Knight shift and the increase in line width to Knight shift anisotropy (KSA).[26,55] The Knight shift occurs due to free electron−nuclear spin interactions resulting in the observed concentration-dependent shift, since $\delta_{obs} = \delta_{CS} + \delta_{KS}$. The values δ_{obs}, δ_{CS}, and δ_{KS} are the observed chemical shift, chemical shift without paramagnetic influence, and the Knight shift contribution, respectively. While the shift is small and potentially within instrumental error, the positive sign of the Knight shift indicates that this interaction occurs through a delocalization mechanism,[26] which would be the expected result for electron−nuclear interactions stemming from free carriers residing in the conduction band. The results support the idea that, in ITO NCs, the Knight shift and KSA changes are directly proportional with Sn concentration, which is consistent with attributing the behavior to the free carrier population at the Fermi level in these PSNCs.[26,56]

In addition to the observed Knight shift and KSA effects induced by free carriers, changes in the T_1 (spin−lattice) and T_2 (spin−spin) relaxation pathways for the Sn(IV) nuclei are anticipated.[29−31] T_1 is related to the Knight shift, while T_2 can be correlated with KSA. It is expected that, as the n-type carrier density in ITO NCs increases with increasing %Sn, the T_1 and T_2 will decrease as a result of paramagnetic relaxation enhancement by the free electrons. However, direct measurements of the T_1 and T_2 of ^{119}Sn are challenging in ITO NCs. T_1 measurements are difficult due to the long T_1 of ^{119}Sn, coupled with the lengthy acquisition times required to obtain suitable spectra at low %Sn. Conversely, the T_2 relaxation rates of these samples are too short to conduct cross-polarization magic-angle spinning (CP-MAS) or Carr−Purcell−Meiboom−Gill (CPMG)[57,58] experiments.

An estimate for the change in T_1 can be obtained from the observed Knight shift (K) through the Knight-Korringa relationship[59,60]

$$T_{1,K}^{-1}(K, T) = \left(\frac{\gamma_n}{\gamma_e}\right)\frac{4\pi k_B T}{\hbar}K^2 \quad (7)$$

where γ_n and γ_e are the gyromagnetic ratios of the nuclear and electronic spins, k_B is the Boltzmann constant, T is the absolute temperature, and $T_{1,K}$ is the Korringa contribution to the spin−

https://dx.doi.org/10.1021/acs.jpcc.0c09448
J. Phys. Chem. C 2020, 124, 28220−28229

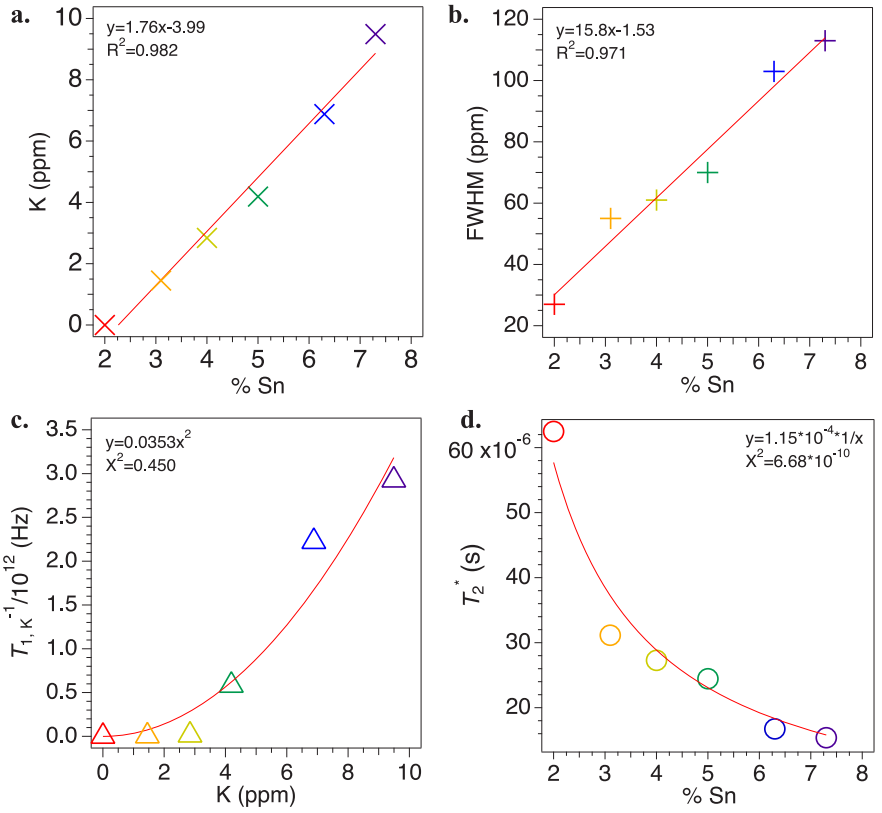

Figure 7. (a) Knight shift of ITO NCs as a function of %Sn. (b) Change in fwhm as a function of %Sn. (c) Knight-Korringa relation estimating the change in T_1 as a function of the Knight shift. (d) Effect of %Sn on T_2*

lattice relaxation. The observed spin−lattice relaxation, $T_{1,K}^{-1}(K,T)$, is a result of the sum of contributions from the paramagnetic relaxation enhancement $T_1^{-1}(K,T)$ and the temperature and Knight shift-independent $T_{1,0}^{-1}$. The relationship will hold for a metallic system, which is consistent with the Fermi carrier density present in an n-type PSNC. A plot of the Knight shift versus the calculated change in $T_{1,K}^{-1}(K,T)$ is shown in Figure 7c. The experimental data follow the predicted K^2 dependence for the Knight-Korringa relationship confirming T_1 is shortened as carrier density increases in ITO. While the shortening of the calculated T_1 is in agreement with the trend seen for $Cu_{2-x}Se$, a p-type PSNC,[29] the magnitude of $T_{1,K}$ for the n-type ITO nanocrystals in this study is small. The small magnitude is believed to be due to the relatively long T_1 for Sn(IV), which has been shown to be between 15 and 80 s,[61,62] compared to that of the ^{77}Se nucleus measured by Millstone on the order of milliseconds. These results indicate that T_1 relaxation is not a good measure for the carrier density for all PSNCs.

The T_2 relaxation is not directly measured, but T_2* can be extracted by relating the line width of the NMR signal to T_2*[63]

$$\Delta\nu_{\text{fwhm}} = \frac{1}{\pi T_2^*} \tag{8}$$

where $\Delta\nu_{\text{fwhm}}$ is the fwhm of the NMR signal measured in hertz. The value of T_2* is related to T_2 by the following expression[64]

$$\frac{1}{T_2^*} = \frac{1}{T_2} + \gamma\Delta B_0 \tag{9}$$

where $\gamma\Delta B_0$ is the change in strength of the local magnetic field. Modern NMR spectrometers exhibit field inhomogeneities below 1 ppm; therefore, for a typical solid-state NMR experiment, the broadening of the signal is primarily due to chemical shift anisotropy, rendering any local changes in magnetic field negligible. This means that, for these experiments, T_2 and T_2* can be considered to be equivalent. In Figure 7d, a plot of T_2* as a function of %Sn shows T_2* is observed to decrease very rapidly at low %Sn levels and then taper off at higher doping concentrations. The extracted value of T_2* is very short in these systems, owing to the large number of free carriers present in n-type ITO NCs. Consistent with a short T_2*, measurement of T_2 using a CPMG[57,58] pulse sequence was not successful. This short transverse relaxation rate for 2.0% and 7.3% ITO samples was insufficient to produce a suitable echo train and produced no discernible signal.

For ITO, the Knight-Korringa relation shows little change with increasing free carrier concentration due to the nature of the ^{119}Sn isotope. The change in line width due to KSA effects for these samples (from ∼30−115 ppm) is much greater than the resulting Knight shift (∼10 ppm). This signifies that T_2 is a more sensitive probe for carrier density than T_1 for plasmonic ITO NCs. Overall, the observed decrease in T_2 with increasing %Sn confirms the role of carriers at the Fermi level in ITO.

CONCLUSIONS

ITO NCs from 2.0 to 7.3% Sn were synthesized and fully characterized via UV−vis−NIR, FTIR, pXRD, ICP-MS, and TEM and by chemical titrations of the free carriers. The carrier density increases linearly with %Sn within this doping regime,

https://dx.doi.org/10.1021/acs.jpcc.0c09448
J. Phys. Chem. C 2020, 124, 28220−28229

as evidenced by the corresponding change in plasmon frequency and B-M shift. On the basis of the results of the chemical titrations, the Drude model underpredicts the carrier density and the number of carriers generated per incorporated dopant ion, while overpredicting the number of native free carriers in ITO. The B-M shift serves as an accurate predictor of changes in carrier density but severely underestimates the number of free carriers needed to induce a band edge shift. Both the Drude and parabolic band theory models fail to predict accurate values for m^*, as they do not take into account the nonparabolicity of the local band structure with respect to the Fermi level. This can be accounted for by using an advanced effective mass model to examine the LSPR and by applying a correction factor to the value for m^* obtained via B-M analysis. ^{119}Sn ssNMR experiments show that these PSNCs demonstrate line width broadening that is directly proportional to the carrier density of the NCs. A possible Knight shift exhibits the correct sign for a delocalization mechanism, as expected for free carriers present at the Fermi level. The magnitude of any Knight shift in these materials is far smaller than that of $Cu_{2-x}Se$.[29] This is likely due to the differences in the electronic band structure between $Cu_{2-x}Se$ and ITO. The magnitude of a Knight shift is dictated by an interaction of unpaired electrons with the nucleus, which can only occur in orbitals with s-character due to the nonzero probability of the electrons residing at the nucleus.[65] The valence band of $Cu_{2-x}Se$ contains strong contributions from the Se 4s orbitals, for which free holes can strongly interact, causing the large Knight shift.[66,67] The conduction band of ITO is composed mostly of In 5s, 5p, and 4d orbitals, and therefore the free electrons have less interaction with any Sn(IV) orbitals.[68] The correlation of line broadening with free carrier concentration serves as a relative measure of carrier density, which is very useful for systems whose LSPR cannot be fully resolved or those that do not possess a LSPR.

■ ASSOCIATED CONTENT

Supporting Information

The Supporting Information is available free of charge at https://pubs.acs.org/doi/10.1021/acs.jpcc.0c09448.

pXRD and Scherrer analysis for all X% Sn:In_2O_3 to verify consistent size and crystal structure for all doping concentrations. Drude modeling and chemical titration-measured carrier densities for each sample. FTIR spectra of 2.0−7.3% ITO NCs. Plots of LSPR frequency and optical bandgap versus %Sn. TEM micrograph and distribution analysis to verify the accuracy of sizes calculated via Scherrer and nanocrystal morphology. ^{19}F NMR of $NOBF_4$ solution and $NOBF_4$ titration measurements for 2.0−7.3% ITO NCs (PDF)

■ AUTHOR INFORMATION

Corresponding Author

Geoffrey F. Strouse − *Florida State University, Department of Chemistry & Biochemistry, Tallahassee 32306, Florida, United States;* orcid.org/0000-0003-0841-282X; Email: gstrouse@fsu.edu

Authors

Carl R. Conti III − *Florida State University, Department of Chemistry & Biochemistry, Tallahassee 32306, Florida, United States*

Giovanni Quiroz-Delfi − *Florida State University, Department of Chemistry & Biochemistry, Tallahassee 32306, Florida, United States*

Joanna S. Schwarck − *Florida State University, Department of Chemistry & Biochemistry, Tallahassee 32306, Florida, United States*

Banghao Chen − *Florida State University, Department of Chemistry & Biochemistry, Tallahassee 32306, Florida, United States*

Complete contact information is available at: https://pubs.acs.org/10.1021/acs.jpcc.0c09448

Author Contributions

Synthesis and general characterization of NCs was performed by C.R.C., G.Q.D., and J.S.S. ssNMR experiments were conducted by C.R.C. and B.C. The manuscript was prepared by C.R.C. and G.F.S.

Notes

The authors declare no competing financial interest.

■ ACKNOWLEDGMENTS

G.F.S. wishes to thank the National Science Foundation (DMR-1905757) "Tuning Plasmonic and Magneto-Plasmonic Behavior in 4-d Transition Metal Doped Indium Oxide" for funding. ssNMR studies were conducted using a spectrometer supported by the National Science Foundation (NSF) (CHE-1126587). A portion of this work was performed at the National High Magnetic Field Laboratory, which is supported by the NSF Cooperative Agreement (DMR-1644779) and the state of Florida. We also thank Drs. R. Schurko and A. Paravastu for discussions about the interpretation of the ssNMR spectra.

■ REFERENCES

(1) Mendelsberg, R. J.; Garcia, G.; Li, H.; Manna, L.; Milliron, D. J. Understanding the Plasmon Resonance in Ensembles of Degenerately Doped Semiconductor Nanocrystals. *J. Phys. Chem. C* **2012**, *116* (22), 12226−12231.

(2) Balitskii, O. A.; Sytnyk, M.; Stangl, J.; Primetzhofer, D.; Groiss, H.; Heiss, W. Tuning the Localized Surface Plasmon Resonance in $Cu_{2-x}Se$ Nanocrystals by Postsynthetic Ligand Exchange. *ACS Appl. Mater. Interfaces* **2014**, *6* (20), 17770−17775.

(3) Dahlman, C. J.; Agrawal, A.; Staller, C. M.; Adair, J.; Milliron, D. J. Anisotropic Origins of Localized Surface Plasmon Resonance in n-Type Anatase TiO_2 Nanocrystals. *Chem. Mater.* **2019**, *31* (2), 502−511.

(4) Fang, H.; Hegde, M.; Yin, P.; Radovanovic, P. V. Tuning Plasmon Resonance of In_2O_3 Nanocrystals throughout the Mid-Infrared Region by Competition between Electron Activation and Trapping. *Chem. Mater.* **2017**, *29* (11), 4970−4979.

(5) Hartstein, K. H.; Schimpf, A. M.; Salvador, M.; Gamelin, D. R. Cyclotron Splittings in the Plasmon Resonances of Electronically Doped Semiconductor Nanocrystals Probed by Magnetic Circular Dichroism Spectroscopy. *J. Phys. Chem. Lett.* **2017**, *8* (8), 1831−1836.

(6) Luther, J. M.; Jain, P. K.; Ewers, T.; Alivisatos, A. P. Localized surface plasmon resonances arising from free carriers in doped quantum dots. *Nat. Mater.* **2011**, *10* (5), 361−366.

(7) Mattox, M. T.; Coffman, K. D.; Roh, I.; Sims, C.; Urban, J. J. Moving the Plasmon of LaB_6 from IR to Near-IR via Eu-Doping. *Materials* **2018**, *11* (2). DOI: 10.3390/ma11020226

(8) Mattox, T. M.; Ye, X.; Manthiram, K.; Schuck, P. J.; Alivisatos, A. P.; Urban, J. J. Chemical Control of Plasmons in Metal Chalcogenide and Metal Oxide Nanostructures. *Adv. Mater.* **2015**, *27* (38), 5830−5837.

(9) Derkachova, A.; Kolwas, K.; Demchenko, I. Dielectric Function for Gold in Plasmonics Applications: Size Dependence of Plasmon Resonance Frequencies and Damping Rates for Nanospheres. *Plasmonics* **2016**, *11* (3), 941−951.
(10) Link, S.; El-Sayed, M. A. Size and Temperature Dependence of the Plasmon Absorption of Colloidal Gold Nanoparticles. *J. Phys. Chem. B* **1999**, *103* (21), 4212−4217.
(11) Moores, A.; Goettmann, F. The plasmon band in noble metal nanoparticles: an introduction to theory and applications. *New J. Chem.* **2006**, *30* (8), 1121−1132.
(12) Fleischmann, M.; Hendra, P. J.; McQuillan, A. J. Raman spectra of pyridine adsorbed at a silver electrode. *Chem. Phys. Lett.* **1974**, *26* (2), 163−166.
(13) Mogensen, K. B.; Kneipp, K. Size-Dependent Shifts of Plasmon Resonance in Silver Nanoparticle Films Using Controlled Dissolution: Monitoring the Onset of Surface Screening Effects. *J. Phys. Chem. C* **2014**, *118* (48), 28075−28083.
(14) Starowicz, Z.; Wojnarowska-Nowak, R.; Ozga, P.; Sheregii, E. M. The tuning of the plasmon resonance of the metal nanoparticles in terms of the SERS effect. *Colloid Polym. Sci.* **2018**, *296* (6), 1029−1037.
(15) Zhao, T.; Jarrett, J. W.; Johnson, J. S.; Park, K.; Vaia, R. A.; Knappenberger, K. L. Plasmon Dephasing in Gold Nanorods Studied Using Single-Nanoparticle Interferometric Nonlinear Optical Microscopy. *J. Phys. Chem. C* **2016**, *120* (7), 4071−4079.
(16) Zhang, X.; Huang, C.; Wang, M.; Huang, P.; He, X.; Wei, Z. Transient localized surface plasmon induced by femtosecond interband excitation in gold nanoparticles. *Sci. Rep.* **2018**, *8* (1), 10499.
(17) Kravets, V. G.; Kabashin, A. V.; Barnes, W. L.; Grigorenko, A. N. Plasmonic Surface Lattice Resonances: A Review of Properties and Applications. *Chem. Rev.* **2018**, *118* (12), 5912−5951.
(18) Buonsanti, R.; Llordes, A.; Aloni, S.; Helms, B. A.; Milliron, D. J. Tunable Infrared Absorption and Visible Transparency of Colloidal Aluminum-Doped Zinc Oxide Nanocrystals. *Nano Lett.* **2011**, *11* (11), 4706−4710.
(19) Burstein, E. Anomalous Optical Absorption Limit in InSb. *Phys. Rev.* **1954**, *93* (3), 632−633.
(20) Moss, T. S. The Interpretation of the Properties of Indium Antimonide. *Proc. Phys. Soc., London, Sect. B* **1954**, *67*, 775−782.
(21) Mendelsberg, R. J.; Zhu, Y.; Anders, A. Determining the nonparabolicity factor of the CdO conduction band using indium doping and the Drude theory. *J. Phys. D: Appl. Phys.* **2012**, *45* (42), 425302.
(22) Muñoz, M.; Pollak, F. H.; Kahn, M.; Ritter, D.; Kronik, L.; Cohen, G. M. Burstein-Moss shift of n-doped $In_{0.53}Ga_{0.47}As/InP$. *Phys. Rev. B: Condens. Matter Mater. Phys.* **2001**, *63* (23), 233302.
(23) Kim, S.; Park, J.; Kim, S.; Lee, Y.; Ahn, S.; Cho, J.; Ju, M.; Lakshminarayan, N.; Dao, V. A.; Yi, J. Free-carrier absorption and Burstein−Moss shift effect on quantum efficiency in heterojunction silicon solar cells. *Vacuum* **2014**, *108*, 39−44.
(24) Sun, Q. C.; Yadgarov, L.; Rosentsveig, R.; Seifert, G.; Tenne, R.; Musfeldt, J. L. Observation of a Burstein−Moss Shift in Rhenium-Doped MoS_2 Nanoparticles. *ACS Nano* **2013**, *7* (4), 3506−3511.
(25) Bertini, I.; Luchinat, C.; Parigi, G.; Ravera, E. Relaxation. In *NMR of Paramagnetic Molecules,* 2nd ed.; Bertini, I., Luchinat, C., Parigi, G., Ravera, E., Eds.; Elsevier: Boston, MA, 2017; pp 77−126.
(26) Pell, A. J.; Pintacuda, G.; Grey, C. P. Paramagnetic NMR in solution and the solid state. *Prog. Nucl. Magn. Reson. Spectrosc.* **2019**, *111*, 1−271.
(27) Mendelsberg, R. J.; Garcia, G.; Milliron, D. J. Extracting reliable electronic properties from transmission spectra of indium tin oxide thin films and nanocrystal films by careful application of the Drude theory. *J. Appl. Phys.* **2012**, *111* (6), 063515.
(28) Liu, Z.; Beaulac, R. Nature of the Infrared Transition of Colloidal Indium Nitride Nanocrystals: Nonparabolicity Effects on the Plasmonic Behavior of Doped Semiconductor Nanomaterials. *Chem. Mater.* **2017**, *29* (17), 7507−7514.
(29) Marbella, L. E.; Gan, X. Y.; Kaseman, D. C.; Millstone, J. E. Correlating Carrier Density and Emergent Plasmonic Features in Cu2−xSe Nanoparticles. *Nano Lett.* **2017**, *17* (4), 2414−2419.
(30) Levin, E. M. Effects of Ge substitution in GeTe by Ag or Sb on the Seebeck coefficient and carrier concentration derived from ^{125}Te NMR. *Phys. Rev. B: Condens. Matter Mater. Phys.* **2016**, *93* (4), 045209.
(31) Levin, E. M.; Cook, B. A.; Ahn, K.; Kanatzidis, M. G.; Schmidt-Rohr, K. Electronic inhomogeneity and Ag:Sb imbalance of $Ag_{1-y}Pb_{18}Sb_{1+z}Te_{20}$ high performance thermoelectrics elucidated by ^{125}Te and ^{207}Pb NMR. *Phys. Rev. B: Condens. Matter Mater. Phys.* **2009**, *80* (11), 115211.
(32) Tandon, B.; Ghosh, S.; Milliron, D. J. Dopant Selection Strategy for High-Quality Factor Localized Surface Plasmon Resonance from Doped Metal Oxide Nanocrystals. *Chem. Mater.* **2019**, *31* (18), 7752−7760.
(33) Agrawal, A.; Cho, S. H.; Zandi, O.; Ghosh, S.; Johns, R. W.; Milliron, D. J. Localized Surface Plasmon Resonance in Semiconductor Nanocrystals. *Chem. Rev.* **2018**, *118* (6), 3121−3207.
(34) Runnerstrom, E. L.; Llordés, A.; Lounis, S. D.; Milliron, D. J. Nanostructured electrochromic smart windows: traditional materials and NIR-selective plasmonic nanocrystals. *Chem. Commun.* **2014**, *50* (73), 10555−10572.
(35) Xu, J.; Zhang, Y.; Zhai, T.-T.; Kuang, Z.; Li, J.; Wang, Y.; Gao, Z.; Song, Y.-Y.; Xia, X.-H. Electrochromic-Tuned Plasmonics for Photothermal Sterile Window. *ACS Nano* **2018**, *12* (7), 6895−6903.
(36) Lemos de Souza, M.; Pereira dos Santos, D.; Corio, P. Localized surface plasmon resonance enhanced photocatalysis: an experimental and theoretical mechanistic investigation. *RSC Adv.* **2018**, *8* (50), 28753−28762.
(37) Gelle, A.; Moores, A. Water splitting catalyzed by titanium dioxide decorated with plasmonic nanoparticles. *Pure Appl. Chem.* **2017**, *89* (12), 1817−1827.
(38) Wang, S.; Riedinger, A.; Li, H.; Fu, C.; Liu, H.; Li, L.; Liu, T.; Tan, L.; Barthel, M. J.; Pugliese, G.; et al. Plasmonic Copper Sulfide Nanocrystals Exhibiting Near-Infrared Photothermal and Photodynamic Therapeutic Effects. *ACS Nano* **2015**, *9* (2), 1788−1800.
(39) Liu, Z.; Liu, X.; Du, Y.; Ren, J.; Qu, X. Using Plasmonic Copper Sulfide Nanocrystals as Smart Light-Driven Sterilants. *ACS Nano* **2015**, *9* (10), 10335−10346.
(40) Ito, D.; Yokoyama, S.; Zaikova, T.; Masuko, K.; Hutchison, J. E. Synthesis of Ligand-Stabilized Metal Oxide Nanocrystals and Epitaxial Core/Shell Nanocrystals via a Lower-Temperature Esterification Process. *ACS Nano* **2014**, *8* (1), 64−75.
(41) González, G. B.; Mason, T. O.; Quintana, J. P.; Warschkow, O.; Ellis, D. E.; Hwang, J. H.; Hodges, J. P.; Jorgensen, J. D. Defect structure studies of bulk and nano-indium-tin oxide. *J. Appl. Phys.* **2004**, *96* (7), 3912−3920.
(42) Frank, G.; Köstlin, H. Electrical properties and defect model of tin-doped indium oxide layers. *Appl. Phys. A: Solids Surf.* **1982**, *27* (4), 197−206.
(43) Lounis, S. D.; Runnerstrom, E. L.; Llordés, A.; Milliron, D. J. Defect Chemistry and Plasmon Physics of Colloidal Metal Oxide Nanocrystals. *J. Phys. Chem. Lett.* **2014**, *5* (9), 1564−1574.
(44) Zandi, O.; Agrawal, A.; Shearer, A. B.; Reimnitz, L. C.; Dahlman, C. J.; Staller, C. M.; Milliron, D. J. Impacts of surface depletion on the plasmonic properties of doped semiconductor nanocrystals. *Nat. Mater.* **2018**, *17* (8), 710−717.
(45) Jung, J.; Pedersen, T. G. Analysis of plasmonic properties of heavily doped semiconductors using full band structure calculations. *J. Appl. Phys.* **2013**, *113* (11), 114904.
(46) Schleife, A.; Neumann, M. D.; Esser, N.; Galazka, Z.; Gottwald, A.; Nixdorf, J.; Goldhahn, R.; Feneberg, M. Optical properties of In_2O_3 from experiment and first-principles theory: influence of lattice screening. *New J. Phys.* **2018**, *20* (5), 053016.
(47) Bel Hadj Tahar, R.; Ban, T.; Ohya, Y.; Takahashi, Y. Tin doped indium oxide thin films: Electrical properties. *J. Appl. Phys.* **1998**, *83* (5), 2631−2645.

https://dx.doi.org/10.1021/acs.jpcc.0c09448
J. Phys. Chem. C 2020, 124, 28220−28229

(48) Liu, X.; Park, J.; Kang, J.-H.; Yuan, H.; Cui, Y.; Hwang, H. Y.; Brongersma, M. L. Quantification and impact of nonparabolicity of the conduction band of indium tin oxide on its plasmonic properties. *Appl. Phys. Lett.* **2014**, *105* (18), 181117.
(49) Chen, Z.; Zhuo, Y.; Tu, W.; Li, Z.; Ma, X.; Pei, Y.; Wang, W. High mobility indium tin oxide thin film and its application at infrared wavelengths: model and experiment. *Opt. Express* **2018**, *26* (17), 22123−22134.
(50) Tauc, J.; Grigorovici, R.; Vancu, A. Optical Properties and Electronic Structure of Amorphous Germanium. *Phys. Status Solidi B* **1966**, *15* (2), 627−637.
(51) Khusayfan, N. M.; El-Nahass, M. M. Study of Structure and Electro-Optical Characteristics of Indium Tin Oxide Thin Films. *Adv. Condens. Matter Phys.* **2013**, *2013*, 408182.
(52) Gupta, L.; Mansingh, A.; Srivastava, P. K. Band gap narrowing and the band structure of tin-doped indium oxide films. *Thin Solid Films* **1989**, *176* (1), 33−44.
(53) Wang, L.; Kefalidis, C. E.; Roisnel, T.; Sinbandhit, S.; Maron, L.; Carpentier, J.-F.; Sarazin, Y. Structure vs ^{119}Sn NMR Chemical Shift in Three-Coordinated Tin(II) Complexes: Experimental Data and Predictive DFT Computations. *Organometallics* **2015**, *34* (11), 2139−2150.
(54) Hamaed, H.; Johnston, K. E.; Cooper, B. F. T.; Terskikh, V. V.; Ye, E.; Macdonald, C. L. B.; Arnold, D. C.; Schurko, R. W. A ^{115}In solid-state NMR study of low oxidation-state indium complexes. *Chemical Science* **2014**, *5* (3), 982−995.
(55) Townes, C. H.; Herring, C.; Knight, W. D. The Effect of Electronic Paramagnetism on Nuclear Magnetic Resonance Frequencies in Metals. *Phys. Rev.* **1950**, *77* (6), 852−853.
(56) Rubens, A.; deCastro, B.; Schumacher, R. T. Knight-Shift Anisotropy in Cubic Crystals. *Phys. Rev. B* **1973**, *7* (1), 105−118.
(57) Carr, H. Y.; Purcell, E. M. Effects of Diffusion on Free Precession in Nuclear Magnetic Resonance Experiments. *Phys. Rev.* **1954**, *94* (3), 630−638.
(58) Meiboom, S.; Gill, D. Modified Spin-Echo Method for Measuring Nuclear Relaxation Times. *Rev. Sci. Instrum.* **1958**, *29* (8), 688−691.
(59) Abraham, R. J. Principles of magnetic resonance. C. P. Slichter. Springer, Berlin, 1990, ISBN 3 540 5057 6, 640 pages, DM89.00. *Magn. Reson. Chem.* **1990**, *28* (12), 1078−1078.
(60) Cho, S. H.; Ghosh, S.; Berkson, Z. J.; Hachtel, J. A.; Shi, J.; Zhao, X.; Reimnitz, L. C.; Dahlman, C. J.; Ho, Y.; Yang, A.; et al. Syntheses of Colloidal F:In_2O_3 Cubes: Fluorine-Induced Faceting and Infrared Plasmonic Response. *Chem. Mater.* **2019**, *31* (7), 2661−2676.
(61) Dey, T.; Khuntia, P.; Mahajan, A. V.; Kumar, N.; Sundaresan, A. ^{119}Sn NMR probe of magnetic fluctuations in SnO_2 nanoparticles. *EPL (Europhysics Letters)* **2011**, *96* (6), 67008.
(62) Tunstall, D. P.; Patou, S.; Liu, R. S.; Kao, Y. H. Size effects in the NMR of SnO_2 powders. *Mater. Res. Bull.* **1999**, *34* (10), 1513−1520.
(63) Szántay, C., Jr NMR and the uncertainty principle: How to and how not to interpret homogeneous line broadening and pulse nonselectivity. I. The fundamentals. *Concepts Magn. Reson., Part A* **2007**, *30A* (6), 309−348.
(64) Chavhan, G. B.; Babyn, P. S.; Thomas, B.; Shroff, M. M.; Haacke, E. M. Principles, Techniques, and Applications of T_2*-based MR Imaging and Its Special Applications. *Radio Graphics* **2009**, *29* (5), 1433−1449.
(65) Weiss, A. G. S. Carter, L. H. Bennett, D. J. Kahan: Metallic Shifts in NMR, A review of theory and comprehensive critical data compilation of metallic materials. Part I—IV (Progress in Materials Science, Vol. 20, Editors: B. Chalmers, J. W. Christian, T. B. Massalski), Pergamon Press, Oxford, New York, Toronto, Sidney, Paris, Frankfurt 1977, pp. 2350, Preis: $300,—. *Berichte der Bunsengesellschaft für physikalische Chemie* **1977**, *81* (8), 779−780.
(66) Milman, V. Klockmannite, CuSe: structure, properties and phase stability from it ab initio modeling. *Acta Crystallographica Section B* **2002**, *58* (3), 437−447, DOI: 10.1107/S0108768102003269.
(67) Tyagi, K.; Gahtori, B.; Bathula, S.; Auluck, S.; Dhar, A. Band structure and transport studies of copper selenide: An efficient thermoelectric material. *Appl. Phys. Lett.* **2014**, *105* (17), 173905.
(68) Mryasov, O. N.; Freeman, A. J. Electronic band structure of indium tin oxide and criteria for transparent conducting behavior. *Phys. Rev. B: Condens. Matter Mater. Phys.* **2001**, *64* (23), 233111.

https://dx.doi.org/10.1021/acs.jpcc.0c09448
J. Phys. Chem. C 2020, 124, 28220−28229